Journal of Alloys and Compounds 1051 (2026) 186017

Contents lists available at ScienceDirect

Journal of Alloys and Compounds

journal homepage: www.elsevier.com/locate/jalcom

Ductile WTaNbHf refractory medium-entropy alloy with excellent oxidation resistance at 1473 K

Guoming Yi [a,b], Huanyu Mo [a,b], Yangbin Guo [a,b], Zhongheng Diao [a,b], Jinyong Mo [c], Qianqian Wang [a,b,d,*], Juan Kuang [a,b,*], Gaopeng Zou [a,b], Bo Sun [a,b], Bingjie Wang [a,b], Baolong Shen [a,b,*]

[a] School of Materials Science and Engineering, Jiangsu Key Laboratory for Advanced Metallic Materials, Southeast University, Nanjing 211189, China
[b] Ministry of Education Key Laboratory of Structure and Thermal Protection for High-Speed Aircraft, Southeast University, Nanjing 211189, China
[c] School of Material Science and Engineering, Chongqing University of Technology, Chongqing 400054, China
[d] Jiangsu Key Laboratory of Advanced Structural Materials and Application Technology, Nanjing Institute of Technology, Nanjing 211167, China

ARTICLE INFO

Keywords:
Refractory high-entropy alloy
Mechanical property
High temperature
Oxidation resistance

ABSTRACT

Refractory high-entropy and medium-entropy alloys (RHEAs/RMEAs) are attractive for ultra-high-temperature applications, but the practical application is severely limited by poor oxidation resistance and extreme room-temperature brittleness. In this work, a $(WTaNb)_{55}Hf_{45}$ refractory medium-entropy alloy with excellent oxidation resistance at 1473 K and large fracture strain (26 %) at room temperature was designed. The formation of a dense and stable oxide layer containing $Hf_6Ta_2O_{17}$ when exposed to the oxidizing environment at 1473 K led to excellent oxidation resistance. Superior room-temperature ductility is attributed to the combined effects of the coherent interface, the lamellar morphology, and the significantly reduced bulk modulus. This work provides a strategy to simultaneously improve the high-temperature oxidation resistance and the room-temperature plasticity of refractory medium-entropy alloys.

1. Introduction

Refractory high/medium-entropy alloys (RH/MEAs) are considered as the promising high-temperature materials for the aerospace industry as they provide not only excellent mechanical and chemical performance at extremely high temperatures, including high strength, good wear and corrosion resistance, but also a wide scope of composition design [1,2]. However, the inadequate high-temperature oxidation resistance of refractory elements and their alloys constitutes a major barrier to their high-temperature application, a challenge that persists in refractory high-entropy alloys (RHEAs) despite their enhanced mechanical properties.

For the first two RHEAs, MoNbTaW and MoNbTaVW, reported in 2010 by Senkov et al., all the constituent elements are easily oxidized at elevated temperatures [3]. MoO_3 and WO_3 evaporate at 795 °C and 1000 °C, respectively. The evaporation of these oxides results in a porous structure, which facilitates the diffusion of oxygen and accelerates the failure of the alloy. Although the Ta_2O_5 and Nb_2O_5 won't evaporate until 1375 °C, their expansion causes cracks in the alloy matrix. Preparing oxidation-resistant coating is an effective method to improve the oxidation resistance of RHEAs, i. e. the preparation of $(NbMoTaW)Si_2$ silicide coating protected the NbMoTaW RHEA from oxidation at 1300 °C for 24 h [4], and further modification by yttrium made the coating withstand ablation up to 2100 °C [5]. However, the degradation of the coating can lead to the catastrophic failure of the RHEAs. Consequently, the rational design of RHEAs with superior intrinsic oxidation resistance constitutes a fundamental prerequisite for fully exploiting their exceptional high-temperature performance. Alloying with elements like Al, Si, and Cr is a proven strategy to enhance oxidation resistance by forming protective oxide layer, but this often comes at the cost of reduced mechanical performance, particularly ductility and sometimes strength [6–8]. The addition of only 0.1 at% Si resulted in a significant decrease in the ductility of TiVNbTa from 14 % to 1.4 % due to the formation of Laves phase [8]. In addition, it was reported that the binary Hf-Ta alloy has outstanding oxidation resistance due to the formation of a dense $Hf_6Ta_2O_{17}$ oxide layer, which limits the oxygen diffusion and serves as a

* Corresponding authors at: School of Materials Science and Engineering, Jiangsu Key Laboratory for Advanced Metallic Materials, Southeast University, Nanjing 211189, China.
E-mail addresses: qwang678@seu.edu.cn (Q. Wang), 230208750@seu.edu.cn (J. Kuang), blshen@seu.edu.cn (B. Shen).

https://doi.org/10.1016/j.jallcom.2026.186017
Received 31 October 2025; Received in revised form 21 December 2025; Accepted 5 January 2026
Available online 5 January 2026

protective layer. The $Hf_6Ta_2O_{17}$ oxide also adheres well to the substrate and is thermal shock resistant [9]. Thus, the addition of the Hf element is promising in improving the oxidation resistance of the RHEAs.

Apart from inadequate oxidation resistance, the poor room-temperature ductility of RHEAs significantly hinders their cold processing and limits structural applications requiring deformation tolerance. $Nb_{25}Mo_{25}Ta_{25}W_{25}$ and $V_{20}Nb_{20}Mo_{20}Ta_{20}W_{20}$ alloys showed excellent thermal stability and high yield strength at high temperatures, but their plastic strain only reached about 2.0 % and 1.5 %, respectively [10]. The poor ductility can lead to cracks at the beginning of deformation. Alloying with ductile elements represents a highly effective strategy for enhancing the ductility of RHEAs. With the addition of Ti, the single-phase BCC NbTaVTi RHEA achieved a compressive strain exceeding 50 % [11]. The TaNbHfZrTi RHEA demonstrated exceptional room-temperature plasticity through the substitution of Mo/W with more ductile Hf, Zr, and Ti elements [12,13]. But the strategy seriously deteriorates their high-temperature strength, i.e., TaNbHfZrTi has only 92 MPa strength at 1200 ºC [14]. Improving the solid solution effect is one of the most effective methods to increase the strength of alloys at room and high temperatures. Enhancement in both strength and ductility was achieved by introducing interstitial oxygen elements into the TiZrHfNb RHEA by forming ordered oxygen complexes [15], and designing negative mixing enthalpy solid solutions [16]. Furthermore, the incorporation of secondary phases in HEA has become a widely adopted strengthening strategy, where deliberately induced microstructural heterogeneity enhances the strength. By increasing Nb and Mo segregation, a heterogeneous-structured $Nb_{45}Mo_{45}Ta_5W_5$ RHEA was developed, exhibiting enhanced room-temperature compressive plasticity of 9.0 % while maintaining high yield strength of 415 MPa at 1873 K [17]. Theoretical calculation indicated that the addition of Hf in NbMoTaW RHEA enhanced the lattice strain greatly and finally induced the formation of a dual BCC phase structure, both of which contribute to the improved strength and ductility of the RHEA [18]. Incorporating the Hf element characterized by low shear-to-bulk modulus into RH/MEAs generates large lattice strain and facilitates secondary phase precipitation, thereby potentially improving the ambient-temperature mechanical performance of alloys.

In this work, Hf with different content is introduced to the NbMoTaW HEA to replace Mo to improve its oxidation resistance and mechanical properties. The arc melted $(WTaNb)_{100-x}Hf_x$ (x = 0, 15, 30, 45, 60 at%) are denoted as Hf0, Hf15, Hf30, Hf45, and Hf60, respectively. The microstructure evolution of the $(WTaNb)_{100-x}Hf_x$ alloys was studied. The oxidation behavior at high temperature, mechanical properties, and the corresponding underlying mechanisms were thoroughly investigated.

2. Materials and methods

The $(WTaNb)_{100-x}Hf_x$ (x = 0, 15, 30, 45, 60 at%) alloys were prepared by arc-melting a mixture of pure Ta, W, Nb, and Hf in a titanium-gettered argon atmosphere. The purities of Ta, W, Nb, and Hf elements are higher than 99.95 wt%. To ensure the chemical homogeneity, the raw material particles were placed by the order of melting point from high to low, and the ingots were flipped over and remelted six times with a melting current of 250–700 A. To prepare samples for compressive tests, the cylindrical samples with a diameter of 2 mm and a height of 4 mm were cut from the ingots by electric-discharged machining [19,20]. The upper and lower faces of all samples were carefully polished with different sandpapers to ensure the uniformity. In addition, a correction method can also be implemented to improve the accuracy of compression data, particularly for small-sized samples [21]. The compression tests were performed using a universal testing machine (Instron 6025) at room temperature with a nominal strain rate of 10^{-3} s^{-1}. Compression tests at 1473 K were conducted in a vacuum furnace with a Zwick KAPPA 100 dynamic thermal simulation testing machine under argon atmosphere. After being soaked at 1473 K for 10 min, the sample was compressed with a strain rate of 10^{-3} s^{-1}, and then cooled in the furnace.

The phases of $(WTaNb)_{100-x}Hf_x$ alloys were analyzed by X-ray diffraction (XRD, Bruker D8-Discover) using Cu-K_α radiation. The fracture surface morphology and grain size distribution were analyzed by scanning electron microscopy (SEM, FEI Sirion 200). For EBSD analysis, the samples were first prepared through 6-hour vibratory polishing (Buehler Vibromet 2) using nanoscale SiO_2 suspension in intermediate frequency mode, followed by scanning with a 0.3 μm step size. The nanostructure of the samples was investigated by a high-resolution transmission electron microscope (TEM, Talos F200X) operated at 200 kV. Atomic number contrast images were collected using the high-angle annular dark field (HAADF) detectors. Energy dispersive X-ray spectroscopy (EDS) mapping was performed at 200 kV. The samples for TEM analysis were thinned using an Ion Beam Thinner (GATAN-691) under the liquid nitrogen cooling condition.

Thermo-Calc (release 2021a) together with the TCHEA4.2 database was adopted to map the phase stability of the $(WTaNb)_{100-x}Hf_x$ (x = 0, 15, 30, 45, 60 at%) alloys under the constraint of full thermodynamic equilibrium. The database, which unifies 26 metallic elements and delivers self-consistent Gibbs-energy descriptions for all plausible phases, has been validated as reliable in the literature [22,23]. These functions were parametrized from critical evaluations of all available binary data and a wide selection of ternary sub-systems, ensuring reliable extrapolation to higher-order compositions. By minimizing the total Gibbs energy of the alloy system, the CALPHAD approach embedded in Thermo-Calc delivers quantitative predictions of equilibrium phase fractions, transformation temperatures, and solidification paths for $(WTaNb)_{100-x}Hf_x$ (x = 0, 15, 30, 45, 60 at%) alloys.

3. Results and discussion

3.1. Microstructure of alloys

The phase structure of $(WTaNb)_{100-x}Hf_x$ alloys was investigated by XRD, as shown in Fig. 1a. A single body-centered cubic (BCC) phase is found within both the Hf0 and Hf15 alloys, while all the diffraction peaks shift left after adding 15 at% Hf. With further increment of Hf content, a hexagonal close-packed (HCP) phase appears in Hf30, Hf45, and Hf60 alloys. The lattice constant of the BCC phase increases continuously from 3.25 Å for Hf0–3.43 Å for Hf60, indicating the enhanced lattice distortion. This comes from the larger atomic size of Hf, as the atomic size of Hf (1.59 Å) is much larger than Ta (1.48 Å), W (1.41 Å), and Nb (1.48 Å). It was reported that the BCC structure with severe distortion is the nucleation site of the HCP phase [24]. Based on their theory, the first step of generating the HCP phase is the formation of clusters rich in HCP-favorable elements, such as Hf, to reduce the nucleation barrier for BCC to HCP transformation. Besides, the Ta, W, and Nb elements are BCC stable elements, while the Hf element is an HCP stable element [25]. Thus, it is reasonable that the addition of Hf leads to the precipitation of HCP phase.

To reveal the thermodynamically preferred microstructure, the phase diagrams of $(WTaNb)_{100-x}Hf_x$ alloys at the equilibrium state were calculated. As shown in Fig. 1b, for Hf0 alloy, a single BCC phase is solidified from the melt, and no phase transformation occurs during cooling. For Hf15, Hf30, and Hf45 alloys (Fig. 1c, d, and e), the formation of the BCC phase from the melt is also observed during the solidification process, except that the solidification temperature decreases with increasing Hf content. For these three alloys, the BCC phase is only stable above 1560 K, and starts to transform to the HCP phase below this temperature. Interestingly, for Hf30 and Hf45 alloys, in the early stage of the phase transformation, a BCC2 phase precipitates from the BCC phase and then dissolves within a short temperature range. At 500 K, all three alloys exhibit a dual phase structure with BCC and HCP with different fractions. The mass fraction of BCC and HCP in Hf45 alloy is approximately 44 % and 56 %, respectively. As shown in Fig. 1f, Hf60 shows a totally different solidification and phase transformation

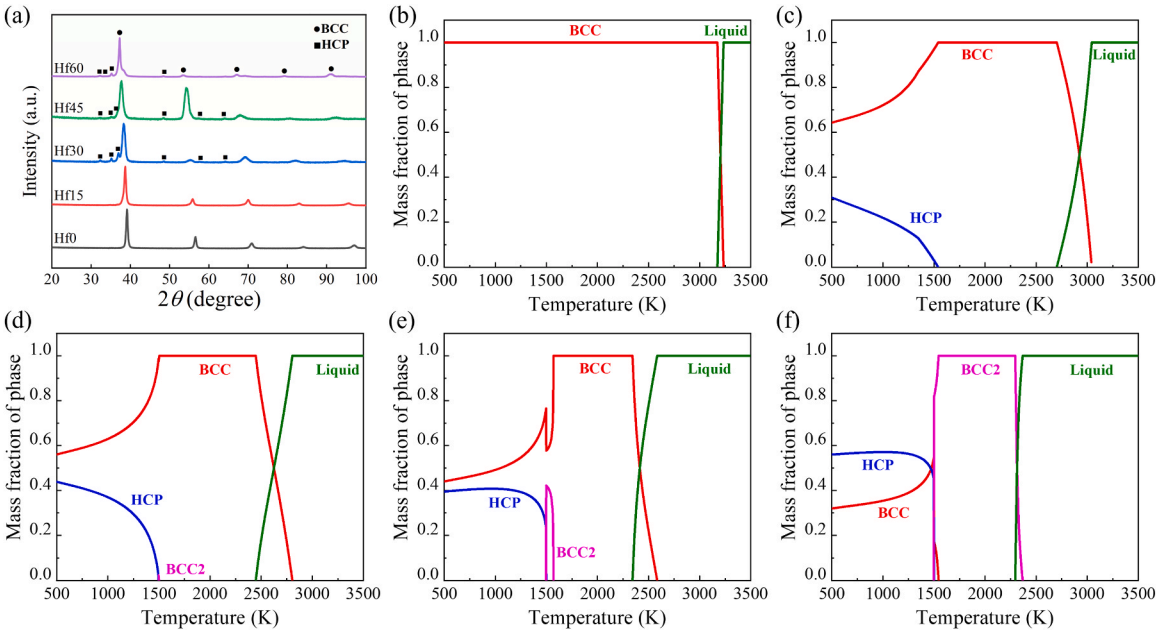

Fig. 1. (a) XRD patterns of the alloys with different Hf contents; calculated phase diagrams of (b) Hf0, (c) Hf15, (d) Hf30, (e) Hf45, and (f) Hf60.

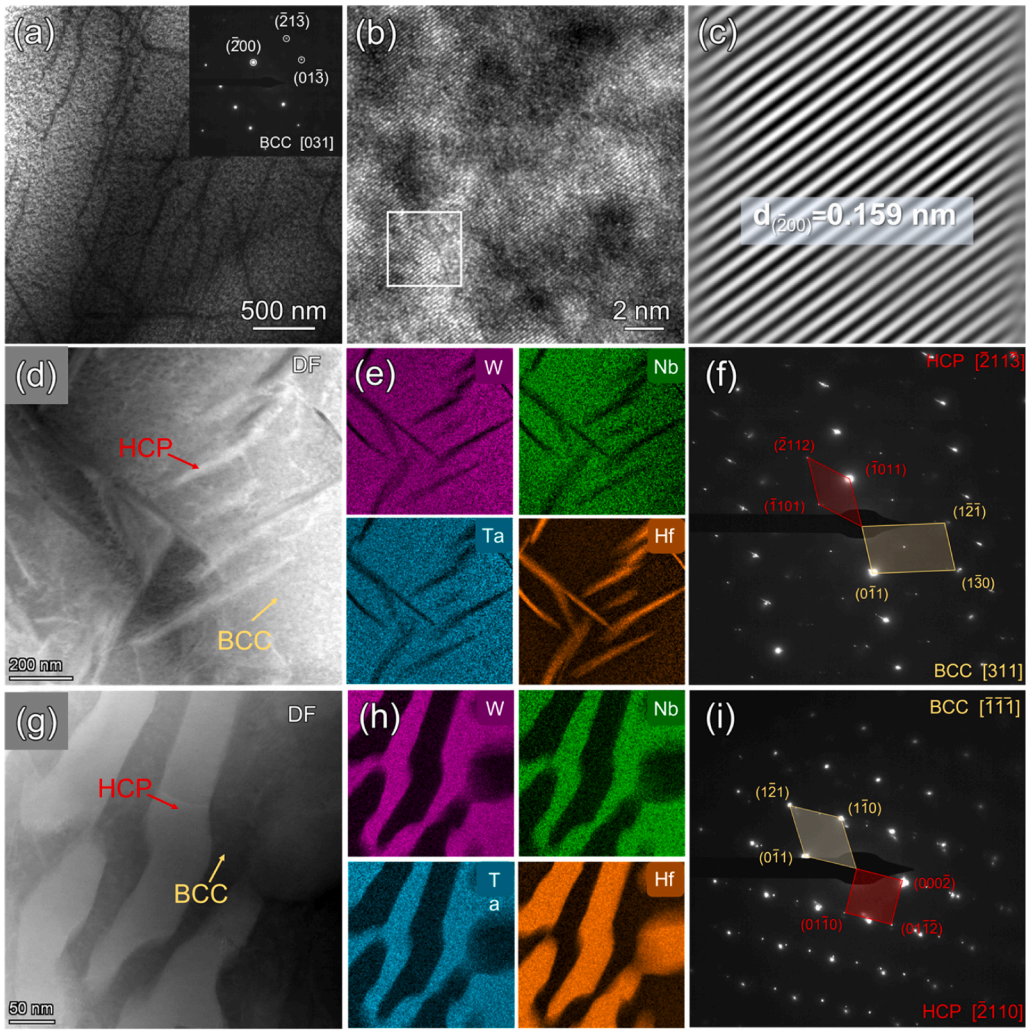

Fig. 2. TEM analyses of the as-cast alloys. (a) DF and SAED images of Hf0; (b) HRTEM image of Hf0; (c) IFFT image of Hf0; (d) DF image of Hf15; (e) EDS analyses of Hf15; (f) SAED image of Hf15; (g) DF image of Hf30; (h) EDS analyses of Hf30; (i) SAED image of Hf30.

process, which forms a BCC2 phase from liquid at around 2500 K and then completely decomposes into BCC and HCP phases at 1500 K. Although the arc melting method used in this work is far from reaching the equilibrium state due to the rapid cooling rate, the overall trend of the phase structure of the alloys can be drawn from the above analyses [26,27].

The microstructure of Hf0, Hf15, and Hf30 alloys is shown in Fig. 2. As shown in the dark field TEM in Fig. 2a, the Hf0 alloy exhibits a single BCC phase with low-density dislocations, and the selected area electron diffraction (SAED) pattern in the inset indicates the BCC phase is disordered. The high-resolution TEM image in Fig. 2b further confirms that the BCC phase has a relatively complete lattice arrangement and low lattice distortion. The FFT-IFFT image in Fig. 2c shows a complete lattice with little crystalline defect. The crystal plane spacing is 0.159 nm, corresponding to the crystal plane of BCC ($\bar{2}00$). As shown in Fig. 2d, the Hf15 alloy exhibits a dual-phase structure with needle-like phase distributed in the matrix. The EDS results in Fig. 2e reveal that the needle-like phase is rich in Hf, while the matrix is rich in Ta, W, and Nb. The SAED pattern in Fig. 2f shows a disordered BCC phase and an ordered HCP phase, as the superlattice diffraction spots can be observed (indicated by the red circles). This is consistent with the results predicted by Thermo-Calc, but different from the XRD result. The volume fraction of the HCP phase is probably too low to be detected by the XRD. As Hf is an HCP stable element, the needle-like structure is the HCP phase, and the matrix is BCC. In order to evaluate the boundary relationship, the mismatching degree ($\overline{\delta^{(hkl)s}_{(hkl)n}}$) was calculated according to the Bramfitt lattice matching theory [28]

$$\overline{\delta^{(hkl)s}_{(hkl)n}} = \sum_{1}^{3} \frac{\left| \left(d_{[uvw]^i_s} \cos\theta\right) - d_{[uvw]^i_n} \right|}{d_{[uvw]^i_n}} \times 100\% \qquad (1)$$

where d represents the planar spacing, and θ is the included angle between the $[uvw]_s$ and $[uvw]_n$. The mismatching degree between the HCP and BCC phases is 11.31 %, indicating the formation of semi-coherent phase boundaries. Matching degree factors of the phase interface between BCC and HCP are listed in Table S1. As shown in Fig. 2g, the microstructure of Hf30 alloy shows a similar structure of Hf15, with a disordered BCC matrix and ordered HCP phase. However, the width of the HCP phase is much larger than the needle-like structure in Hf15. Based on the calculated mismatching degree of 19 %, the BCC and HCP phases in the Hf30 alloy exhibit a semi-coherent interfacial relationship.

As shown in Fig. 3a, the Hf45 alloy shows a similar structure to that of the Hf30 alloy. But the lamellar thickness of the Hf-rich phase is different, with a thickness of 20–60 nm in width. The SAED pattern shown in the inset confirms the coexistence of disordered BCC and ordered HCP phases, maintaining a coherent interface, with a lattice mismatching degree of 2.07 %. The HRTEM image of the as-cast Hf45 alloy (Fig. 2c) shows the interface of the two phases. The mismatch of atomic arrangement is very low even at the interface. Besides, a small number of stacking faults (SFs) and dislocations appear near the BCC matrix and the coherent HCP phase. The microstructure of Hf45 alloy is further analyzed by EBSD and shown in Fig. S1. The phase distribution diagram in Fig. S1a confirms the dual phase structure with BCC matrix phase and a distributed HCP phase. The size of HCP is below 4 μm, and the content is 11.8 % of the overall alloy. The IPF map in Fig. S1b shows that the BCC grains are close to equiaxed, and the grain size is about 20–50 μm. The appearance of fine HCP phases can also be observed, distributed inside the BCC grain or at the grain boundaries.

As shown in the HAADF images in Figs. 3d and 3e, no lamellar structure is observed in Hf60. Based on the EDS results in Fig. 3f, three phases are observed in the alloy with different compositions. The matrix contains Ta, W, Nb, and Hf elements, while a blocky Hf-rich phase precipitates along the grain boundary, and a W-rich phase appears inside the Hf-rich phase. As the SAED results in Fig. 3e_1, e_2, and e_3 show, the W-rich phase, Hf-rich phase, and the matrix are BCC2, HCP, and BCC, respectively. According to the equilibrium phase diagram of Hf60 in Fig. 1f, the BCC2 phase precipitates at about 2300 K and decomposes into a disordered BCC matrix and HCP phase at about 1600 K, which means the BCC2 phase won't exist at room temperature if solidified at an extremely slow cooling rate. The above results show that part of the BCC2 phase wasn't decomposed due to the fast-cooling rate of the water-

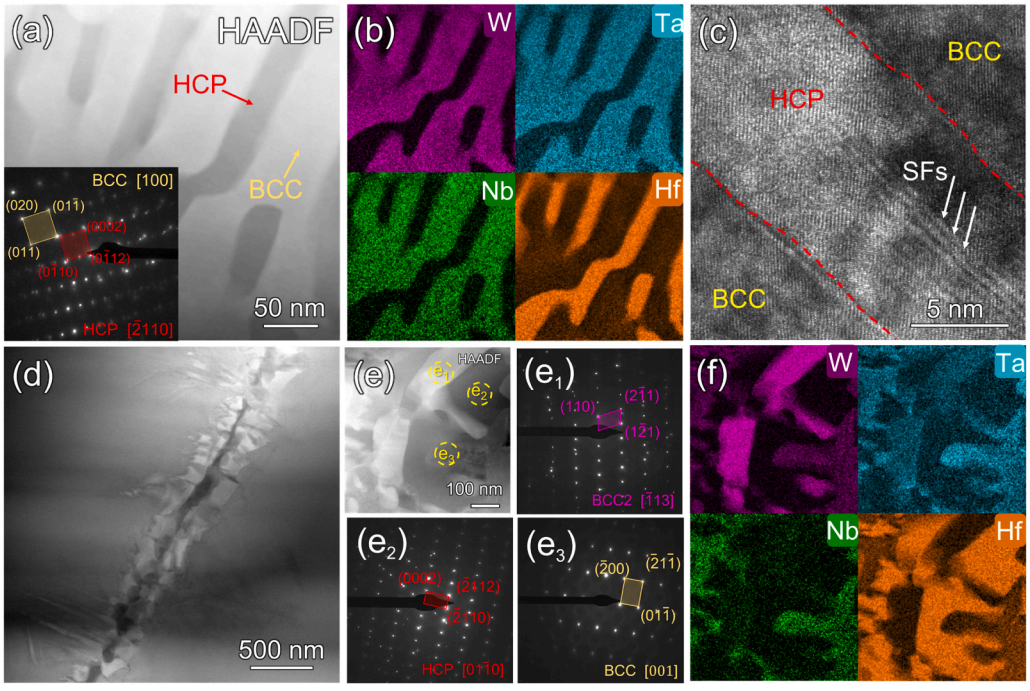

Fig. 3. TEM analyses of the as-cast alloys. (a) HAADF and SAED images of Hf45; (b) EDS analyses of Hf45; (c) HRTEM image of the interface of BCC and HCP in Hf45; (d) and (e) TEM and HAADF images of Hf60; (e_1)-(e_3) SAED patterns of different phases in Hf60; (f) EDS analyses of (e).

cooled copper mold used in vacuum arc melting. Besides, no coherent relationship between the HCP phase and the matrix BCC phase is observed.

3.2. Oxidation behavior at 1473 K

To investigate the oxidation behavior of the Hf0 and Hf45 alloys, oxidation tests were conducted on the two alloys at 1473 K. The macroscopic morphology of the oxidized alloys is depicted in Fig. 4. Exposed in air only for 0.5 h, obvious cracks originating from volume expansion are observed on the corners of the Hf0 alloy. After 1.5 h of oxidation exposure, the Hf0 alloy manifests pronounced swelling-induced deformation in its oxide layer, resulting in total loss of structural integrity. The residual substrate observed in the core region is completely oxidized after 3 h. In contrast, the Hf45 alloy retains its structural integrity throughout the entire 30 h oxidation, while cracks in the corners emerge after 12 h exposure. The oxide surface remains smooth with no bulging or spallation observed during oxidation.

The oxidation mass gain curves of the Hf0 and Hf45 alloys at 1473 K are illustrated in Fig. 5a. The mass gain per unit area of the Hf0 alloy increases rapidly, exhibiting a linear trend, indicating its poor oxidation resistance. In contrast, the mass gain of the Hf45 alloy obeys a parabolic law, indicating that the oxide growth is controlled by cation diffusion [29,30]. The maximum mass gain at 30 h reaches 88 mg/cm^2, which is only about a quarter of that of Hf0. In contrast, the two representative RHEAs NbMoTaW [4] and NbMoTAWV [31] completely failed after being oxidized at 1573 K and 1473 K for only 0.5 h (65 mg/cm^2 and 123 mg/cm^2, respectively). Compared with other RHEAs listed in Table S2, Hf45 alloy demonstrates superior performance by maintaining structural integrity at relatively high oxidation temperatures while exhibiting a comparatively lower mass gain. The phase compositions of oxide on Hf0 and Hf45 alloy after oxidation were analyzed by XRD and shown in Figs. 5c and 5d. For Hf0, the predominant formation comprises Ta_2O_5 and multicomponent oxides $Nb_{14}W_3O_{44}$. Fig. 5d reveals the presence of three distinct phases (HfO_2, $Nb_{14}W_3O_{44}$, and $Hf_6Ta_2O_{17}$) on the oxidized surface of Hf45 alloy. The $Hf_6Ta_2O_{17}$ phase, formed through a solid phase reaction between HfO_2 and Ta_2O_5 at elevated temperatures, exhibits exceptional thermal stability and strong oxygen inhibition ability [32]. In addition, the Ellingham diagram for the metal-oxide reactions in Fig. 5b shows the relative thermodynamic stabilities of the oxides that form in a multicomponent system [33]. The low and adjacent positions of HfO_2 and Ta_2O_5 indicate that their oxides form preferentially and sequentially during oxidation, thereby promoting the solid-state reaction between them to form the dense-structured $Hf_6Ta_2O_{17}$.

Fig. 6 shows the surface morphology of the Hf0 and Hf45 alloys after oxidation for different time. As depicted in Fig. 6a, significant spallation of the oxide layer is observed on the Hf0 alloy surface after 0.5 h oxidation, with numerous fragmented oxide flakes detaching from the substrate. The retained oxide exhibits extensive surface cracks (Fig. 6b), beneath which lies a loose internal oxide layer (Fig. 6c). In contrast, oxidized in air for the same 0.5 h, a continuous and compact oxide layer formed on Hf45 with no crack observed (Fig. 6d). As the oxidation time prolonged to 5 h (Fig. 6e) and 24 h (Fig. 6f), microcracks emerged within the oxide, progressively increasing in number without causing severe cracking or spallation. High-magnification images (Fig. 6g and h) reveal the presence of fine oxide particles uniformly distributed on the oxide layer surface, which are likely formed in the later stage of oxidation. After 24 h oxidation, two distinct contrast regions of oxide particles are identified in Fig. 6i. Further EDS analysis confirms that the two phases observed in the inset of Fig. 6i correspond to Hf-rich oxide (Point 1: Hf-24.82 at%, Nb-5.57 at%, Ta-5.74 at%, and O-63.86 at%) and Ta, Nb-enriched oxide phases (Point 2: Hf-8.25 at%, Nb-18.26 at%, Ta-10.21 at%, W-5.11 at%, and O-58.17 at%), respectively. At elevated temperatures, HfO_2 and Ta_2O_5 can undergo a solid phase reaction in Ta-rich regions to form $Hf_6Ta_2O_{17}$ with excellent phase stability, which leads to superior oxygen inhibition ability [32,34].

Fig. 7 shows the cross-section morphology of Hf0 and Hf45 alloys after oxidation for different time. As shown in Fig. 7a, a typical laminated structure feature can be observed after 0.5 h of oxidation, with the oxide remaining adherent to the substrate. The extension of the oxidation time to 1 h leads to a dramatic increase in the oxide layer thickness from 200 μm to 340 μm, accompanied by the development of substantial and large-sized cracks, which ultimately brought the entire layer to the verge of spallation from the substrate (Fig. 7b). The severe oxidation of Hf0 alloy after short-term exposure is due to the formation of Ta_2O_5 and Nb_2O_5 oxides, whose detrimental volume expansion fails to provide protective effects and directly induces catastrophic material failure [35,36]. Despite the thickness of the oxide layer on the Hf45 alloy growing from 107 μm to 674 μm over 24 h of oxidation, no crack is observed either within the oxide layer or at the oxide/substrate interface (Fig. 7c-e). As shown in Fig. 7e, the dense oxide layer shows the sign of degradation at 24 h, with a small portion of the outer layer transitioning into a porous oxide structure. The EDS line scanning result in Fig. 7f shows that Hf, Nb, Ta, W, and O are evenly distributed in the outer cross-section regions of the oxide layers. However, the O content significantly decreases in the inner oxide layer, indicating that the inward diffusion of O is effectively hindered by the oxide layer (Points 4 and 5).

3.3. Mechanical behavior

The room-temperature engineering compressive stress–strain curves of the as-cast $(WTaNb)_{100-x}Hf_x$ HEAs are shown in Fig. 8a. Hf0 alloy exhibits a yield strength of ~1211 MPa with ultimate compressive strength of ~1741 MPa, and fracture strain of 13 %. Increasing the Hf

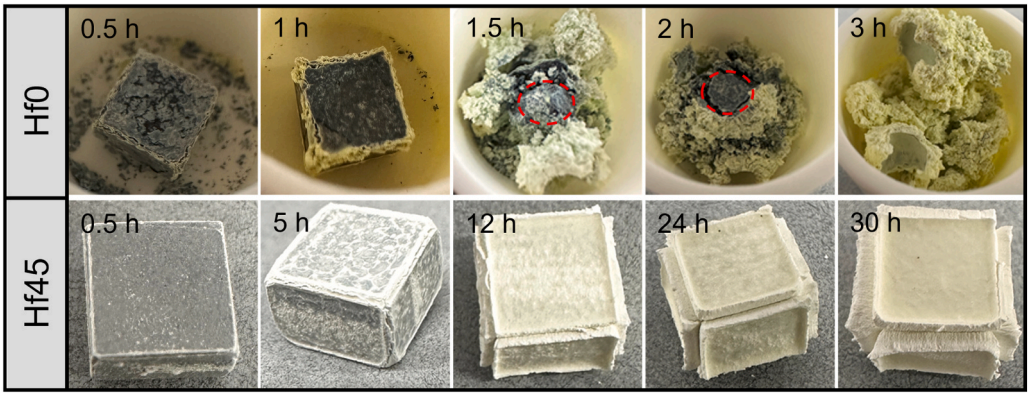

Fig. 4. Macroscopic images of Hf0 and Hf45 alloys oxidized at 1473 K.

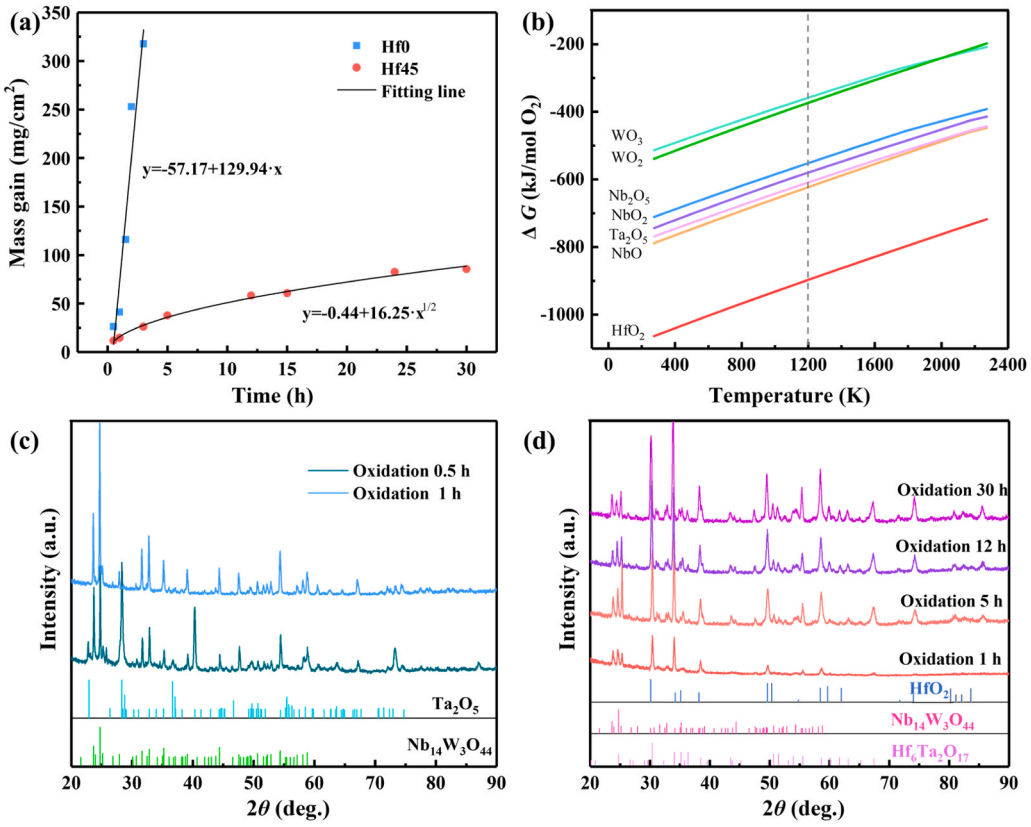

Fig. 5. Oxidation behavior of Hf0 and Hf45 alloys oxidized at 1473 K. (a) Mass gain curves; (b) Ellingham diagram for the metal-oxide reactions; (c) and (d) XRD patterns of oxidized Hf0 and Hf45.

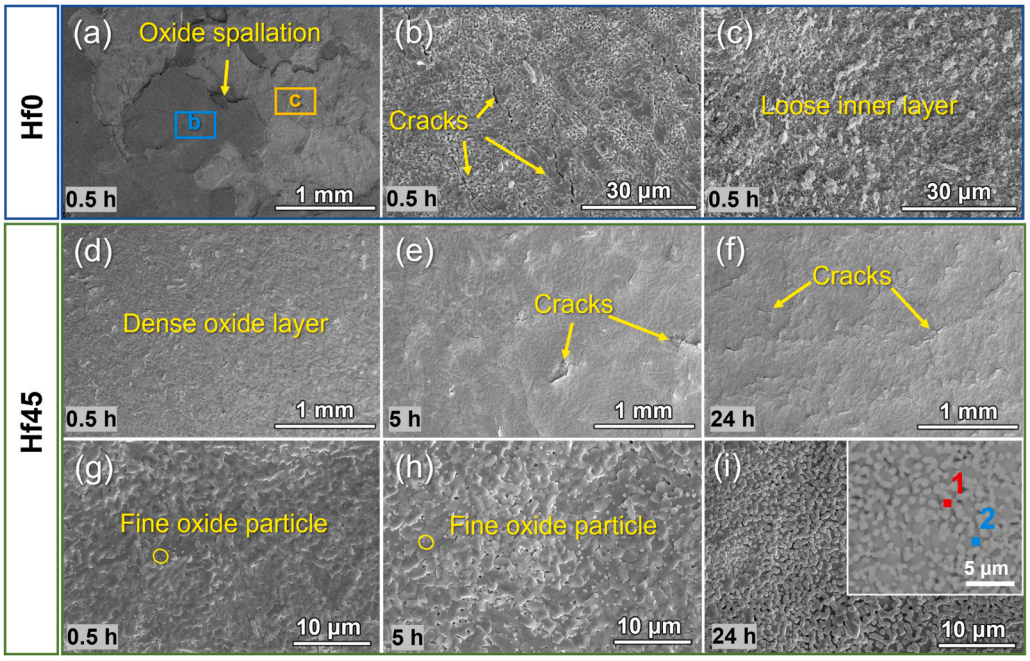

Fig. 6. Surface morphology after oxidation analyzed by SEM. (a)-(c) Hf0 oxidized for 0.5 h; Hf45 oxidized for (d) 0.5 h, (e) 5 h, and (f) 24 h; (g)-(i) Magnified images of (d)-(e), the inset in (i) is back scattered SEM.

element significantly strengthens the Hf15 and Hf30 alloys, with the yield strength increasing to 1634 and 2067 MPa, respectively. Moreover, the fracture strain in both alloys is slightly promoted to 14 % and 17 %, respectively. The Hf45 alloy displays a remarkable combination of strength and ductility with a yield strength of 2228 MPa, ultimate compressive strength of 3135 MPa, and fracture strain of 26 %. Compared to the RHEAs alloying oxidation-resistant elements in Table S3, Hf45 retains superior ductility while achieving enhanced

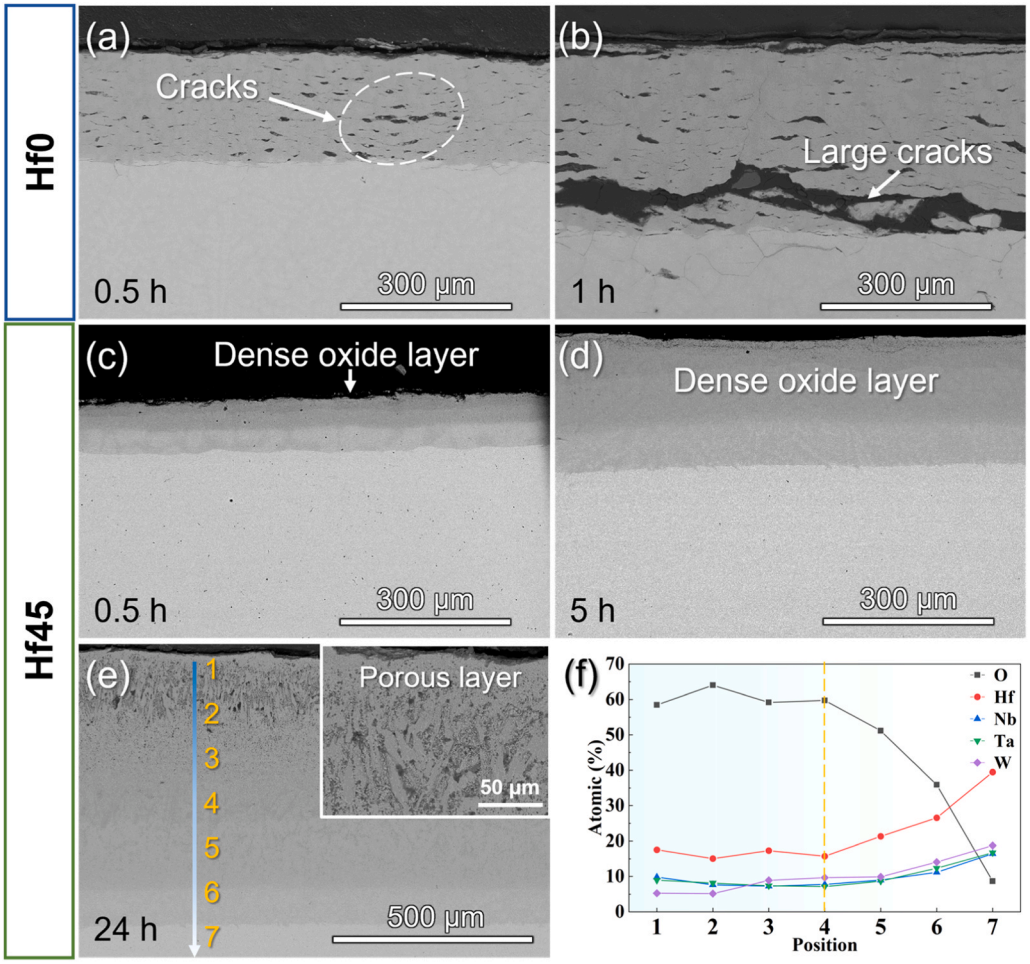

Fig. 7. Cross-section morphology after oxidation analyzed by SEM. Hf0 oxidized for (a) 0.5 h, (b) 1 h; Hf45 oxidized for (c) 0.5 h, (d) 5 h, (e) 24 h; (f) EDS line scanning results of Hf45 oxidized for 24 h.

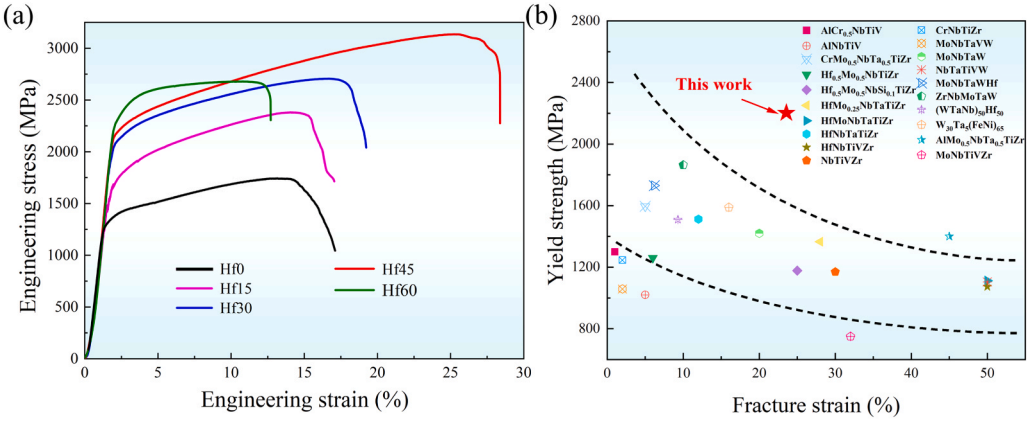

Fig. 8. Mechanical behavior. (a) Room-temperature engineering compressive stress–strain curves of $(WTaNb)_{100-x}Hf_x$ alloys; (b) Yield strength and plastic strain of Hf45 compared with other reported HEAs.

oxidation resistance. As for the Hf60 alloy, although the yield strength continues to increase to 2308 MPa, its fracture strain decreases to 12 %, which makes the ultimate compressive strength decrease to 2679 MPa. The strain-hardening rate ($d\sigma/d\varepsilon$) curves of the HEAs derived from the corresponding true stress-strain curves are shown in Fig. S2. The curve of the Hf0 alloy exhibits a rapid decrease, indicating its significantly inferior ductility. Upon introducing a minor Hf addition (Hf15 and Hf30 alloys), the decrease stage of the work hardening curve is slightly delayed. The formation of semi-coherent interfaces resulted in a notable enhancement in the work hardening rates of Hf15 and Hf30 alloys. Notably, increasing Hf content to 45 at%, the formation of coherent interfaces between the BCC and the HCP phases resulted in a decreased strain hardening rate, an extended strain hardening range, and consequently improved ductility. However, upon excessive Hf addition, the Hf60 alloy exhibits a pronounced deterioration in work hardening rate, which consequently leads to compromised ductility. In addition, the

yield strength and fracture strain of Hf45 are compared with other HEAs that have been reported, as shown in Fig. 8b (The detailed data of the alloys are listed in Table S4). The Hf45 has a yield strength that is higher than most of the reported HEAs, together with a relatively large fracture strain.

The SEM images of the fracture surface after compressive tests for the $(WTaNb)_{100-x}Hf_x$ HEAs are shown in Fig. 9a-e. Only vein patterns are observed on the fracture surface of Hf0, indicating a typical brittle fracture. With the increase of Hf content, dimples appear on the fracture surface of Hf15 and become the major fracture morphology for Hf30 and Hf45, which is consistent with the increase of fracture strain. For Hf60, only vein patterns resulting from brittle fracture are observed. A polished fracture surface of Hf45 is shown in Fig. 9f, evidencing transgranular crack propagation, further confirming the ductile fracture.

The microstructure of Hf45 alloy after 20 % fracture strain is analyzed by TEM, as shown in Fig. 10. Based on the HAADF image in Fig. 10a, the BCC and HCP phases show cooperative deformation, and bending occurs at the interfaces of the dual phases. The morphology of the HCP phase changes to needle-like. It can be speculated that a large amount of strain is absorbed at the interface, and extremely high strain energy is stored. The EDS results shown in Fig. 10b indicate that the HCP phase maintains a much higher content of Hf. The SAED pattern in Fig. 10c confirms that the two phases maintain a coherent relationship after deformation. The tendency to form rings of the diffraction spots results from the large plastic deformation of the grains. As shown in the TEM image in Fig. 10d, a large number of dislocations are stacked and multiplied, forming complex structures such as forest dislocations and dislocation cells. The interlacing and entanglement of dislocations lead to the strengthening of the alloy. Some dislocations can cut through the interface between the HCP phase and the matrix BCC phase in their slip direction, which is caused by the coherent interface. This can alleviate the stress concentration at the interface, delay the crack initiation process, and prolong the work hardening stage of the alloy [37,38]. The dislocation density in the BCC phase is much higher than that in the HCP phase when it is located at the interface between the disordered BCC and the HCP (Fig. 10e). There is no significant quantitative difference in dislocation content within the alloys when both sides of the interface are BCC matrix phases (Fig. 10f). This indicates that the BCC phase bear more strain during the process of external compressive stress. The HRTEM images (Fig. 10g and 10 g_1) and SAED pattern (Fig. 10 g_2) of the interface prove that the coherent relationship between the HCP phase and the BCC phase is maintained after 20 % fracture strain.

The origin of the simultaneously enhanced strength and plasticity of Hf45 alloy is as follows. The strength increase can be attributed to the lattice distortion induced by the solid solution of the large atomic size of the Hf element, together with the second-phase strengthening from the HCP phase. The increase in plasticity can be explained by two aspects. Firstly, the lamellar arrangement of the two-phase, similar to some eutectic structures, can obviously absorb the strain at the two-phase interface to delay the crack generation process [39–41]. The dislocation density can then be increased up to the maximum limit of the alloy, which in turn increases the strength without sacrificing ductility at room temperature. Secondly, the coherent interface of the two phases can slow down the stress concentration process [41]. The dislocation can cut through the two-phase coherent interface without being hindered by the interface stress field. Thirdly, the overall bulk modulus decreases continuously with the increase of the Hf element, and thus leads to a larger fracture strain. The decrease of the fracture strain in Hf60 results from the tremendous morphology change of the HCP phase and the appearance of W-rich BCC2 phase, which may accelerate the initiation of the cracks.

The compressive mechanical behavior of Hf45 at 1473 K is analyzed, with the stress-strain curve shown in Fig. S3. The Hf45 alloy maintains a relatively high yield strength of 456 MPa at 1473 K. The deformation process of Hf45 can be categorized into three stages: work hardening, dynamic softening, and steady state stages. For the work hardening stage, the dislocation interaction leads to the formation of high-density dislocations as well as the formation of low-angle grain boundaries and subgrain microstructure, which impedes the deformation, and thus the stress increases continuously. For the dynamic softening stage, with the increase of dislocation density, the distortion energy of the alloy increases, and the driving force for the dynamic recovery and recrystallization is accumulated. At the same time, the dislocation climbing and cross-slip are induced, so the softening is dominated by dynamic recovery, and recrystallization occurs [42–44]. In addition, if the phase transition occurs in the alloy, a part of the stress can be released, which is manifested as a decrease in the stress value on the stress-strain curve. Then the strengthening induced by dislocation interaction and the second phase competes with the stress softening dominated by dynamic recrystallization and phase transition. When the two reach an equilibrium, the stress doesn't change much with increasing strain, and thus the alloy deformation is observed to be at the steady state stage.

It should be noted that the use of small specimens in compression testing may compromise the accuracy of measured mechanical properties, due to the disproportionate contribution of non-specimen displacements (frame compliance, contact gaps, and stress concentration at interfaces) to the total machine-recorded displacement and the insufficient grain number within the cross-section [21]. This leads to an

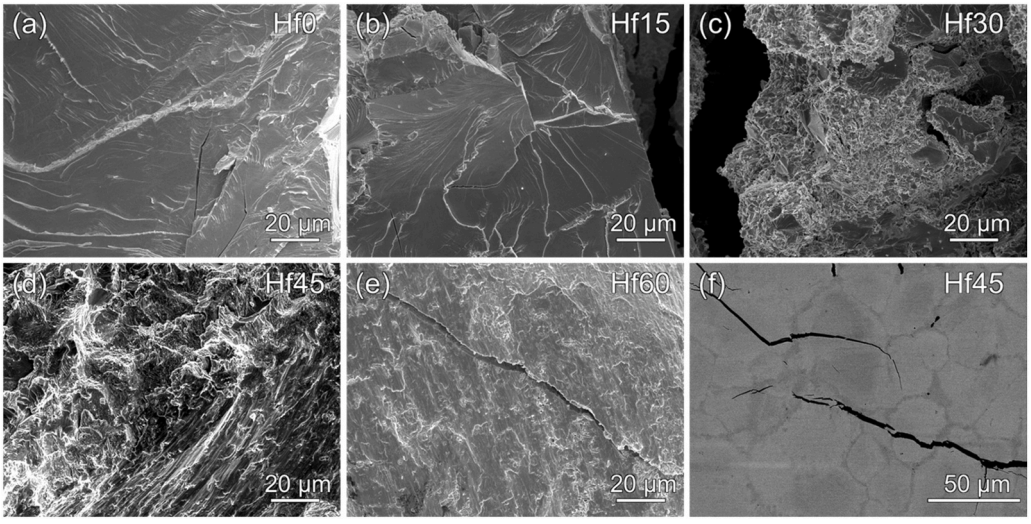

Fig. 9. SEM images of the fracture surface after compressive tests. (a)-(e) Hf0-Hf60; (f) Polished fracture surface of Hf45.

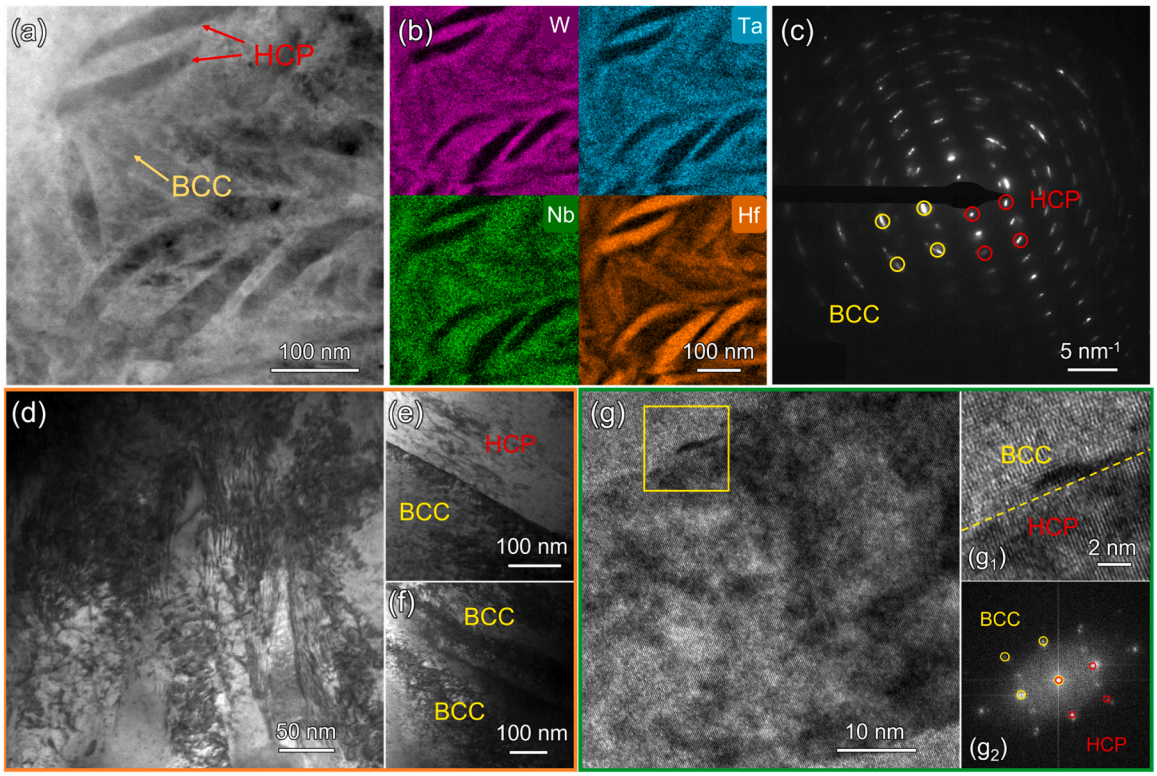

Fig. 10. Microstructure analyses of Hf45 with 20 % plastic strain. (a) HAADF image; (b) EDS analysis; (c) SAED pattern; (d) TEM image of dislocations; (e) Interface of BCC and HCP; (f) Interface of BCC matrix phases; (g) and (g_1) HRTEM images, (g_2) SAED pattern of g_1.

underestimation of the elastic modulus and an overestimation of fracture strain. For RHEAs, the cylindrical specimens with diameters of 2–4 mm and a length-to-diameter ratio of 2 are commonly used in evaluating compressive mechanical properties. The adoption of 2 × 4 mm cylindrical specimens in this work is primarily based on the following considerations: (1) The NbTaWHf system's large melting point differences (>1200 K) between elements lead to elemental segregation and inhomogeneous as-cast microstructures, where smaller specimens reduce non-equilibrium solidification effects. (2) Our previous studies have demonstrated negligible differences in room- and elevated-temperature yield strength and plastic strain between 2 × 4 mm and 4 × 8 mm specimens [19]. (3) The 2 × 4 mm configuration is more prevalently adopted, facilitating performance comparison under consistent baseline conditions. The mechanical behavior of centimeter-scale specimens requires further systematic investigation in future studies.

4. Conclusion

In this work, a $(WTaNb)_{55}Hf_{45}$ alloy with excellent oxidation resistance and large plasticity at room temperature was designed. The addition of Hf significantly enhances the oxidation resistance of NbTaW alloy by promoting the formation of a dense $Hf_6Ta_2O_{17}$-dominated oxide layer, which effectively suppresses oxygen inward diffusion and reduces crack formation. The coherent interface between the HCP nano lamellar and the BCC phase contributes to the improved plasticity at room temperature. This work provides a strategy to design materials with superior high-temperature oxidation resistance and excellent room-temperature plasticity.

CRediT authorship contribution statement

Zhongheng Diao: Methodology. **Jinyong Mo:** Methodology. **Huanyu Mo:** Writing – review & editing, Investigation, Data curation. **Yangbin Guo:** Investigation, Formal analysis, Data curation. **Gaopeng Zou:** Investigation, Conceptualization. **Qianqian Wang:** Writing – review & editing, Supervision, Project administration, Funding acquisition, Conceptualization. **Juan Kuang:** Investigation, Data curation, Conceptualization. **Baolong Shen:** Supervision, Project administration, Funding acquisition, Conceptualization. **Guoming Yi:** Writing – original draft, Methodology, Investigation. **Bo Sun:** Conceptualization. **Bingjie Wang:** Methodology.

Declaration of Competing Interest

The authors declare that they have no known competing financial interests or personal relationships that could have appeared to influence the work reported in this paper.

Acknowledgments

This work is supported by the National Natural Science Foundation of China (52571183, 52231005), the Jiangsu Provincial Key Research and Development Program (BE2021088), Opening Project of Jiangsu Key Laboratory for Advanced Metallic Materials (AMM2020A01, AMM2024A02, AMM2023B05), and Jiangsu Key Laboratory of Advanced Structural Materials and Application Technology (ASMA202302).

Appendix A. Supporting information

Supplementary data associated with this article can be found in the online version at doi:10.1016/j.jallcom.2026.186017.

Data availability

Data will be made available on request.

References

[1] J.-W. Yeh, S.-K. Chen, S.-J. Lin, J.-Y. Gan, T.-S. Chin, T.-T. Shun, C.-H. Tsau, S.-Y. Chang, Nanostructured high-entropy alloys with multiple principal elements: novel alloy design concepts and outcomes, Adv. Eng. Mater. 6 (2004) 299–303, https://doi.org/10.1002/adem.200300567.

[2] B. Cantor, I.T.H. Chang, P. Knight, A.J.B. Vincent, Microstructural development in equiatomic multicomponent alloys, Mater. Sci. Eng. A 375–377 (2004) 213–218, https://doi.org/10.1016/j.msea.2003.10.257.

[3] O.N. Senkov, G.B. Wilks, D.B. Miracle, C.P. Chuang, P.K. Liaw, Refractory high-entropy alloys, Intermetallics 18 (2010) 1758–1765, https://doi.org/10.1016/j.intermet.2010.05.014.

[4] J. Kuang, P. Zhang, Q. Wang, Z. Hu, X. Liang, B. Shen, Formation and oxidation behavior of refractory high-entropy silicide (NbMoTaW)Si_2 coating, Corros. Sci. 198 (2022) 110134, https://doi.org/10.1016/j.corsci.2022.110134.

[5] J. Kuang, Q. Wang, Z. Jia, G. Yi, B. Sun, Y. Yang, L. Sun, P. Zhang, P. He, Y. Xing, X. Liang, Y. Lu, B. Shen, Ablation-resistant yttrium-modified high-entropy refractory metal silicide (NbMoTaW)Si_2 coating for oxidizing environments up to 2100 °C, Mater. Today 80 (2024) 156–166, https://doi.org/10.1016/j.mattod.2024.08.012.

[6] F. Wang, T. Yang, S. Lin, Y. Zhong, J. Tang, L. Zhao, L. Li, J. Wu, C. Wang, W. Dang, Y. Wang, T. Fu, H. Li, H. Zhao, P. Niu, T. Yuan, Aluminum content regulation for strength-toughness synergy and defect suppression in laser powder bed fusion of $NbTa_{0.5}$Ti-based refractory high-entropy alloys, Mater. Sci. Eng. A 945 (2025) 149072, https://doi.org/10.1016/j.msea.2025.149072.

[7] Z. Geng, J. Peng, W. Lu, Z. Xu, Q. Shen, C. Wang, L. Zhang, Concurrent strength-ductility enhancement of as-cast $Al_{0.5}Mo_{0.5}NbTa_{0.5}TiZr$ refractory high entropy alloys via cr alloying and the underlying mechanism, J. Alloy. Compd. 1036 (2025) 181708, https://doi.org/10.1016/j.jallcom.2025.181708.

[8] Z.Q. Xu, Z.L. Ma, Y. Tan, X.W. Cheng, Designing TiVNbTaSi refractory high-entropy alloys with ambient tensile ductility, Scr. Mater. 206 (2022) 114230, https://doi.org/10.1016/j.scriptamat.2021.114230.

[9] Y. Yang, J.H. Perepezko, C. Zhang, Oxidation synthesis of $Hf_6Ta_2O_{17}$ superstructures, Mater. Chem. Phys. 197 (2017) 154–162, https://doi.org/10.1016/j.matchemphys.2017.04.055.

[10] O.N. Senkov, G.B. Wilks, J.M. Scott, D.B. Miracle, Mechanical properties of $Nb_{25}Mo_{25}Ta_{25}W_{25}$ and $V_{20}Nb_{20}Mo_{20}Ta_{20}W_{20}$ refractory high entropy alloys, Intermetallics 19 (2011) 698–706, https://doi.org/10.1016/j.intermet.2011.01.004.

[11] H.W. Yao, J.W. Qiao, M.C. Gao, J.A. Hawk, S.G. Ma, H.F. Zhou, Y. Zhang, NbTaV-(Ti,W) refractory high-entropy alloys: experiments and modeling, Mater. Sci. Eng. A 674 (2016) 203–211, https://doi.org/10.1016/j.msea.2016.07.102.

[12] O.N. Senkov, A.L. Pilchak, S.L. Semiatin, Effect of cold deformation and annealing on the microstructure and tensile properties of a HfNbTaTiZr refractory high entropy alloy, Metall. Mater. Trans. A 49 (2018) 2876–2892, https://doi.org/10.1007/s11661-018-4646-8.

[13] O.N. Senkov, J.M. Scott, S.V. Senkova, D.B. Miracle, C.F. Woodward, Microstructure and room temperature properties of a high-entropy TaNbHfZrTi alloy, J. Alloy. Compd. 509 (2011) 6043–6048, https://doi.org/10.1016/j.jallcom.2011.02.171.

[14] O.N. Senkov, J.M. Scott, S.V. Senkova, F. Meisenkothen, D.B. Miracle, C. F. Woodward, Microstructure and elevated temperature properties of a refractory TaNbHfZrTi alloy, J. Mater. Sci. 47 (2012) 4062–4074, https://doi.org/10.1007/s10853-012-6260-2.

[15] Z. Lei, X. Liu, Y. Wu, H. Wang, S. Jiang, S. Wang, X. Hui, Y. Wu, B. Gault, P. Kontis, D. Raabe, L. Gu, Q. Zhang, H. Chen, H. Wang, J. Liu, K. An, Q. Zeng, T.-G. Nieh, Z. Lu, Enhanced strength and ductility in a high-entropy alloy via ordered oxygen complexes, Nature 563 (2018) 546–550, https://doi.org/10.1038/s41586-018-0685-y.

[16] Z. An, A. Li, S. Mao, T. Yang, L. Zhu, R. Wang, Z. Wu, B. Zhang, R. Shao, C. Jiang, B. Cao, C. Shi, Y. Ren, C. Liu, H. Long, J. Zhang, W. Li, F. He, L. Sun, J. Zhao, L. Yang, X. Zhou, X. Wei, Y. Chen, Z. Lu, F. Ren, C.-T. Liu, Z. Zhang, X. Han, Negative mixing enthalpy solid solutions deliver high strength and ductility, Nature 625 (2024) 697–702, https://doi.org/10.1038/s41586-023-06894-9.

[17] B. Sun, Q. Wang, J. Mo, B. Wang, X. Liang, B. Shen, Promoted high-temperature strength and room-temperature plasticity synergy by tuning dendrite segregation in NbMoTaW refractory high-entropy alloy, Int. J. Refract. Met. Hard Mater. 118 (2024) 106469, https://doi.org/10.1016/j.ijrmhm.2023.106469.

[18] J. Mo, X. Liang, B. Shen, Y. Wan, H. Mao, Z. Zhang, W. Li, S. Schönecker, L. Vitos, X. Li, Local lattice distortions, phase stability, and mechanical properties of NbMoTaWHf_x alloys: a combined theoretical and experimental study, Comput. Mater. Sci. 217 (2023) 111891, https://doi.org/10.1016/j.commatsci.2022.111891.

[19] B. Sun, B. Wang, Z. Jia, L. Sun, J. Kuang, Q. Wang, G. Sha, X. Liang, B. Shen, Strength-plasticity synergy from ambient to high temperature via gradient-ordering in boride-reinforced WTaV medium-entropy alloy, Nat. Commun. 16 (2025) 11529, https://doi.org/10.1038/s41467-025-66617-8.

[20] B. Sun, J. Mo, Q. Wang, Y. Chen, Z. Zhang, B. Shen, X. Liang, Outstanding specific yield strength of a refractory high-entropy composite at an ultrahigh temperature of 2273 K, J. Mater. Sci. Technol. 166 (2023) 145–154, https://doi.org/10.1016/j.jmst.2023.05.014.

[21] H. He, Z. Xiao, Z. Yang, T. Sun, B. Ma, X. Zhou, T. Guo, W. Wang, J. Fang, Error in compression stress-strain curve recording without extensometer and its correction method for non-standard small-sized specimens, J. Strain Anal. Eng. Des. (2025), https://doi.org/10.1177/03093247251356832.

[22] P.L.J. Conway, T.P.C. Klaver, J. Steggo, E. Ghassemali, High entropy alloys towards industrial applications: high-throughput screening and experimental investigation, Mater. Sci. Eng. A 830 (2022) 142297, https://doi.org/10.1016/j.msea.2021.142297.

[23] A. Manzoni, H. Daoud, S. Mondal, S. van Smaalen, R. Völkl, U. Glatzel, N. Wanderka, Investigation of phases in $Al_{23}Co_{15}Cr_{23}Cu_8Fe_{15}Ni_{16}$ and $Al_8Co_{17}Cr_{17}Cu_8Fe_{17}Ni_{33}$ high entropy alloys and comparison with equilibrium phases predicted by thermo-calc, J. Alloy. Compd. 552 (2013) 430–436, https://doi.org/10.1016/j.jallcom.2012.11.074.

[24] X. Huang, L. Liu, W. Liao, J. Huang, H. Sun, C. Yu, Characterization of nucleation behavior in temperature-induced BCC-to-HCP phase transformation for high entropy alloy, Acta Metall. Sin. (Engl. Lett. 34 (2021) 1546–1556, https://doi.org/10.1007/s40195-021-01282-6.

[25] H. Huang, Y. Wu, J. He, H. Wang, X. Liu, K. An, W. Wu, Z. Lu, Phase-transformation ductilization of brittle high-entropy alloys via metastability engineering, Adv. Mater. 29 (2017) 1701678, https://doi.org/10.1002/adma.201701678.

[26] B. Schuh, B. Völker, J. Todt, N. Schell, L. Perrière, J. Li, J.P. Couzinié, A. Hohenwarter, Thermodynamic instability of a nanocrystalline, single-phase TiZrNbHfTa alloy and its impact on the mechanical properties, Acta Mater. 142 (2018) 201–212, https://doi.org/10.1016/j.actamat.2017.09.035.

[27] C.A. Stewart, R.W. Fonda, K.E. Knipling, Mn-stabilized austenitic steel strengthened by nano-scale β-NiAl (B2), FCC-Cu, and carbides via ICME design, Scr. Mater. 200 (2021) 113903, https://doi.org/10.1016/j.scriptamat.2021.113903.

[28] B.L. Bramfitt, The effect of carbide and nitride additions on the heterogeneous nucleation behavior of liquid iron, Metall. Trans. 1 (1970) 1987–1995, https://doi.org/10.1007/BF02642799.

[29] H. Yi, M. Liang, J. Zhang, B. Yin, J. Huang, F. Qi, Z. Yang, G. Zhou, Q. Jin, J. Chen, Y. Yang, Compositional-structural inhomogeneity and multi-layered oxide film formation on high-entropy alloys, Acta Mater. 296 (2025) 121278, https://doi.org/10.1016/j.actamat.2025.121278.

[30] J. Lu, Y. Chen, H. Zhang, N. Ni, L. Li, L. He, R. Mu, X. Zhao, F. Guo, Y/Hf-doped AlCoCrFeNi high-entropy alloy with ultra oxidation and spallation resistance, Corros. Sci. 166 (2020) 108426, https://doi.org/10.1016/j.corsci.2019.108426.

[31] G. Yi, Y. Ding, Y. Cheng, P. Zhang, X. Wang, X. Liang, Development and oxidation behavior of high entropy silicide (NbMoTaWV)Si_2 coatings on NbMoTaWV alloy, J. Alloy. Compd. 916 (2022) 165384, https://doi.org/10.1016/j.jallcom.2022.165384.

[32] S. He, Y. Liu, Z. Ma, S. Zhu, L. Liu, G. Mu, Y. Li, Study on anti-ablation properties of HfB_2-$TaSi_2$ coatings prepared by atmospheric plasma spraying, J. Alloy. Compd. 999 (2024) 175069, https://doi.org/10.1016/j.jallcom.2024.175069.

[33] L. Backman, E.J. Opila, Thermodynamic assessment of the group IV, V and VI oxides for the design of oxidation resistant multi-principal component materials, J. Eur. Ceram. Soc. 39 (2019) 1796–1802, https://doi.org/10.1016/j.jeurceramsoc.2018.11.004.

[34] C. Zhang, B. Boesl, A. Agarwal, Oxidation resistance of tantalum carbide-hafnium carbide solid solutions under the extreme conditions of a plasma jet, Ceram. Int. 43 (2017) 14798–14806, https://doi.org/10.1016/j.ceramint.2017.07.227.

[35] R. Su, H. Zhang, G. Ouyang, L. Liu, D.D. Johnson, J.H. Perepezko, Oxidation mechanism in a refractory multiple-principal-element alloy at high temperature, Acta Mater. 246 (2023) 118719, https://doi.org/10.1016/j.actamat.2023.118719.

[36] R. Su, H. Zhang, G. Ouyang, L. Liu, W. Nachlas, J. Cui, D.D. Johnson, J. H. Perepezko, Enhanced oxidation resistance of $(Mo_{95}W_5)_{85}Ta_{10}(TiZr)_5$ refractory multi-principal element alloy up to 1300°C, Acta Mater. 215 (2021) 117114, https://doi.org/10.1016/j.actamat.2021.117114.

[37] J.-W. Zhang, S.-M. Liu, W.-Z. Han, Interfaces reduce dislocation loop formation in irradiated nanolayered Zr-2.5Nb, Scr. Mater. 200 (2021) 113902, https://doi.org/10.1016/j.scriptamat.2021.113902.

[38] L. Wang, L. Wang, S. Zhou, Q. Xiao, Y. Xiao, X. Wang, T. Cao, Y. Ren, Y.-J. Liang, L. Wang, Y. Xue, Precipitation and micromechanical behavior of the coherent ordered nanoprecipitation strengthened Al-Cr-Fe-Ni-V high entropy alloy, Acta Mater. 216 (2021) 117121, https://doi.org/10.1016/j.actamat.2021.117121.

[39] X. Liu, X. Zhao, J. Chen, Y. Lv, X. Wang, B. Liu, Y. Liu, Effect of C addition on microstructure and mechanical properties of as-cast HEAs $(Fe_{50}Mn_{30}Co_{10}Cr_{10})_{100-x}C_x$, Mater. Chem. Phys. 254 (2020) 123501, https://doi.org/10.1016/j.matchemphys.2020.123501.

[40] P. Shi, W. Ren, T. Zheng, Z. Ren, X. Hou, J. Peng, P. Hu, Y. Gao, Y. Zhong, P. K. Liaw, Enhanced strength–ductility synergy in ultrafine-grained eutectic high-entropy alloys by inheriting microstructural lamellae, Nat. Commun. 10 (2019) 489, https://doi.org/10.1038/s41467-019-08460-2.

[41] S.Z. Han, E.-A. Choi, S.H. Lim, S. Kim, J. Lee, Alloy design strategies to increase strength and its trade-offs together, Prog. Mater. Sci. 117 (2021) 100720, https://doi.org/10.1016/j.pmatsci.2020.100720.

[42] H. Zhang, K. Zhang, S. Jiang, H. Zhou, C. Zhao, X. Yang, Dynamic recrystallization behavior of a γ′-hardened nickel-based superalloy during hot deformation, J. Alloy. Compd. 623 (2015) 374–385, https://doi.org/10.1016/j.jallcom.2014.11.056.

[43] D.-X. Wen, Y.C. Lin, H.-B. Li, X.-M. Chen, J. Deng, L.-T. Li, Hot deformation behavior and processing map of a typical ni-based superalloy, Mater. Sci. Eng. A 591 (2014) 183–192, https://doi.org/10.1016/j.msea.2013.09.049.

[44] T. Sakai, A. Belyakov, R. Kaibyshev, H. Miura, J.J. Jonas, Dynamic and post-dynamic recrystallization under hot, cold and severe plastic deformation conditions, Prog. Mater. Sci. 60 (2014) 130–207, https://doi.org/10.1016/j.pmatsci.2013.09.002.